Accepted Manuscript in Analytical and Bioanalytical Chemistry

Published citation and link: Lotfi Marchoubeh, M., Cobb, S.J., Abrego Tello, M. et al. Miniaturized probe on polymer SU-8 with array of individually addressable microelectrodes for electrochemical analysis in neural and

other biological tissues. Anal Bioanal Chem 413, 6777-6791 (2021). https://doi.org/10.1007/s00216-021-03327-2

Supplementary Information link: https://static-content.springer.com/esm/art%3A10.1007%2Fs00216-021-03327-

2/MediaObjects/216_2021_3327_MOESM1_ESM.pdf

Miniaturized Probe on Polymer SU-8 with Array of Individually Addressable Microelectrodes

for Electrochemical Analysis in Neural and other Biological Tissues

Mahsa Lotfi Marchoubeh, ^a Samuel J. Cobb, ^b Miguel Abrego Tello, ^a Mengjia Hu, ^a Andrea Jaquins

Gerstl, Elaine M. Robbins, Julie V. Macpherson, Adrian C. Michael and Ingrid Fritsch

a) Department of Chemistry and Biochemistry, University of Arkansas, Fayetteville, 72701, USA,

b) Department of Chemistry, University of Cambridge, CB2 1EW, UK.

c) Department of Chemistry, University of Pittsburgh, Pittsburgh, PA, 15260, USA

d) Department of Chemistry and Centre for Doctoral Training in Diamond Science and Technology,

and Department of Physics, University of Warwick, Coventry, U.K.

*. To whom correspondence should be addressed

Tel: (479) 575-6499

Email: <u>ifritsch@uark.edu</u>

Key words: SU-8 probe, generation-collection, microfabrication, electrochemical analysis, dopamine,

redox cycling

1

Abstract

An SU-8 probe with an array of nine, individually-addressable gold microband electrodes (100 um long, 4 µm wide, separated by 4 µm gaps) was photolithographically fabricated and characterized for detection of low concentrations of chemicals in confined spaces and in vivo studies of biological tissues. The probe's shank (6 mm long, 100 um wide, 100 um thick) is flexible, but exhibits sufficient sharpness and rigidity to be inserted into soft tissue. Laser micromachining was used to define probe geometry into its shape through the SU-8 layers to access an underlying sacrificial aluminum layer that was etched to free the probes from a silicon wafer. Perfusion with fluorescent nanobeads showed that, like a carbon fiber electrode, the probe produced no noticeable damage when inserted into rat brain, in contrast to damage from an inserted microdialysis probe. The individual addressability of the electrodes allows single and multiple electrode activation. Redox cycling is possible, where adjacent electrodes serve as generators (that oxidize or reduce molecules) and collectors (that do the opposite) to amplify signals of small concentrations without background subtraction. Information about electrochemical mechanisms and kinetics may also be obtained. Detection limits for potassium ferricyanide in potassium chloride electrolyte of 2.19, 1.25 and 2.08 µM, and for dopamine in artificial cerebral spinal fluid of 1.94, 1.08 and 5.66 µM for generators alone and for generators and collectors during redox cycling, respectively, were obtained.

Introduction

Major technological advances have been made in the field of electrochemical sensors that are capable of detecting chemicals in confined spaces [1, 2]. However, improving the design of probes so that they may be inserted into tissue and detect small amounts of biological molecules with minimal damage remains an area of need [3]. To address this, we have developed a semi-flexible probe with suitable dimensions that are designed specifically for detection of molecules in vivo and other small volume systems. The probe consists of an array of parallel, individually-addressable microband electrodes that are suitable for redox cycling (generation-collection) experiments where selective activation/deactivation is possible. Redox cycling is a powerful technique that involves diffusional shuttling of molecules between closely spaced electrodes having opposing potentials that oxidize and then re-reduce them [4-7]. Electrochemical signals amplify when the gaps between the electrodes narrow. When performed at steady state, where the potentials of the generators and collectors are held constant, the arrival of an analyte can be detected by redox cycling in real time without needing to subtract a charging current (unlike transient methods) while sustaining the amplified signal. In addition, the monitoring of the currents at the different electrodes, which can be affected by the fate of the molecules while in transit, can lead to quantifying the composition of a sample and a deeper understanding of the kinetics and mechanisms of the chemical system [4, 7, 8].

A significant body of work involving needle-like probes for in vivo analysis focuses on interfacing to, stimulating and understanding brain function [9]. These probes involve different measurement modalities that contribute complementary information and have various specifications. This prior knowledge was drawn upon to design and construct the redox cycling probe described herein. That body of work also offers a context in which to compare the performance of our probe. The sampling

of extracellular fluid with microdialysis probes, for example, allows for extensive chemical analysis, although not in real time, and they can damage tissue while eliciting an immune response that eventually obscures sampling effectiveness [10]. Thus, narrower probes are desirable. Another modality involves wire-like electrodes, one to two orders of magnitude thinner than microdialysis probes, that record voltage pulses associated with real-time firing of neurons but do not acquire chemical information [11]. Direct measurement of chemical changes in real time is also possible at similarly-shaped, carbon fiber electrodes (4-50 µm in diameter) and at microelectrodes patterned on substrates suitable for in vivo insertion [12, 13], but with electrochemical methods like fast scan cyclic voltammetry (FSCV) [14].

This latter approach targets small electroactive molecules, which are detected directly in response to timed stimuli [15]. Electrochemical sensing of other small molecules, often facilitated by enzymes and mediators, have also been reported, but have been deployed to a lesser extent on probes for tissue insertion [16, 17]. Although more challenging to fabricate, probes with multiple, individually-addressable electrodes offer several benefits. These include redundant sensing (in case of failure), spatial mapping, replicate analysis of a single analyte and simultaneous analysis of multiple analytes [18-20].

To our knowledge, there are only two examples of a multi-electrode probe where the electrodes are close enough together for diffusion layers of adjacent sites to overlap on the time scale of the experiment so that redox cycling is possible [12, 21, 22]. Redox cycling on a probe would be especially attractive in a dynamically changing biological system as an alternative to FSCV, where detection of basal levels of chemicals has been a major challenge [14, 15]. While there have been advances in basal dopamine detection at carbon fiber electrodes using fast scan controlled adsorption voltammetry [23] and square wave voltammetry [24], these techniques have much slower timescales than FSCV.

The multielectrode probes suitable for redox cycling have consisted of IDAs and fabricated by photolithography on silicon nitride, but elaborate substrate thinning and etching procedures were used to release them from the substrate [12, 21]. A dual electrode probe that avoids photolithography altogether, involves two, closely spaced carbon fibers [25] and is capable of combining FSCV with amplification because of the short transit time across a 180 nm nanogap. A limitation of IDAs and the electrode configurations is the fixed electrode number and width/gap geometry for a given device. To better understand the effect of diffusion and following chemistry in addition to the feasibility of differentiating between chemicals, individually addressable electrodes are desirable. This is because they offer unique spatio-temporal analysis capabilities. Activation of generator and collector electrodes at various separations from each other has allowed for differential detection of the three catecholamines from each other without fabricating a new device [4, 26].

The choice of the substrate material is particularly important, not only for the application but also in determining the fabrication approach. Silicon-based and ceramic substrates have employed photolithographic techniques to fabricate relatively complex and advanced, multisite neural probes [12, 13, 17, 27, 28]. Despite their advantages, complications with tissue damage during and after insertion of brittle silicon shanks remain a concern. This is mainly due to the mechanical mismatch between the soft neural tissue and the stiff probe. The desire for less rigidity and hardness has led to introduction of polymeric substrates into microfabricated neural probe technology. Parylene [29], polyimide [30] and SU-8 [31] are the most common polymers used to fabricate implantable neural probes.

Of the different polymers investigated, SU-8 is believed to have optimal properties compared to parylene and polyimide. The major setback with these other two polymers is their lack of stiffness, and therefore they easily buckle during insertion into the brain [30, 32]. In addition, polyimide has a

relatively high moisture uptake (~4 wt%) which will ultimately lead to changes in the performance of the electrodes [33]. SU-8 has been shown to exhibit suitable flexibility to minimize tissue damage, and sufficient rigidity for insertion into the brain [34] without mechanical reinforcement. In addition, SU-8's biocompatibility, in terms of cell viability, hemolytic activity, effect of leachates, and histocompatibility has been studied and results suggest suitability for neural implants [35]. Therefore, SU-8 was chosen as a substrate for our probes. Also, photolithography was used in our work to pattern an array of individually-addressable, gold/chromium electrodes spaced apart by only a few micrometers (described further below) on the SU-8 substrate. However, to construct a suitable probe shape that is thin enough for minimal tissue damage can be extremely challenging using photolithography alone. Thus, an alternative approach to shape the substrate was employed here to resolve this complication.

Laser micromachining offers such an alternative route to fabricate complex geometries on the microscale in materials from diamond [36] to polymers that cannot be processed by photolithography [37], or the workflow doesn't allow for it [38], for instance, due to the chemicals or process used interacting adversely with another element of the device. This can streamline device fabrication as the material is cut in a single step as opposed to the several steps required for most photolithography processes, which are usually conducted in a cleanroom environment. Laser micromachining has been used to produce devices as diverse as microelectrodes [38], electrochemical sensors [36], fuel cells [37] and micro-electromechanical systems (MEMS). SU-8 has been processed using excimer laser micromachining to give features on the order of 100 µm [38], and it has been shown that the process does not affect the material's cytotoxicity [39], making it a viable technique for producing electrode arrays for biological applications. Furthermore, the technique is ideal for device prototyping in research environments as the design can be iterated without the time or expense of producing a new

photomask. Consequently, laser micromachining was investigated as a means of defining our distinctive probe shape in SU8.

The work here presents the design and fabrication of a probe on SU-8 that can be easily lifted off a wafer after laser micromachining with a shape that provides ease of connectivity to an edge connector on one end and insertion into tissue on the other. The probe has nine individually addressable, co-planar, microband gold electrodes that were photolithographically fabricated near the tip and can be used to perform generation-collection experiments. Strategic selection of different individual and groups of electrodes acting as generators and collectors can lead to various outcomes, and the experiments can be tailored for maximized generation or collection depending on the goal of the study. Electrochemical characterization of each electrode was performed, and the redox cycling behavior of the electrodes was assessed with the model compound potassium ferricyanide in potassium chloride electrolyte and with dopamine in artificial cerebral spinal fluid and compared to theoretically expected responses. The suitability of the dimensions of the probe shank for insertion into rat brain and extent of tissue damage were also established in anticipation of future studies *in vivo*.

Materials and Methods

Chemicals and Materials

Unless otherwise stated, chemicals were reagent grade and used without further purification. Hexylmethyldisilazane (HMDS), acetone (ACS reagent, \geq 99.5%) and isopropyl alcohol (IPA, \geq 99.7%) were obtained from Sigma Aldrich. Water (ACS reagent grade, 18 M Ω cm or greater) was obtained from Ricca Chemical (Arlington, TX, USA). Dopamine hydrochloride, calcium chloride, sodium dihydrogen phosphate monohydrate, and 4-(2-hydroxyethyl)-1-piperazineethanesulfonic acid (HEPES) (all ACS

grade) were obtained from Alfa Aesar (Ward Hill, MA, USA). Magnesium sulfate, potassium ferricyanide (99.8% pure) and sodium chloride were obtained from EMD Chemicals (Gibbstown, NJ, USA). Sodium hydrogen carbonate was obtained from J.T. Baker (Phillipsburg, NJ, USA). Sodium sulfate was obtained from Aldrich Chemical (St. Louis, MO, USA). D(+)-glucose (anhydrous) and potassium chloride were obtained from BDH/VWR (Radnor, PA, USA). Carbon fiber microelectrodes were constructed from T650 fibers from Cytec LLC (Piedmont, SC, USA) in a borosilicate glass housing from A-M Systems (Sequim, WA, USA) sealed with Spurr Epoxy from Polysciences Inc. (Warrington, PA, USA) with a nichrome lead wire from Goodfellow (Oakdale, PA, USA). Components for artificial cerebrospinal fluid (aCSF, 142 mM NaCl, 1.2 mM CaCl₂, 2.7 mM KCl, 1.0 mM MgCl₂, 2.0 mM NaH₂PO₄, pH 7.4) and phosphate buffered saline (PBS, 137 mM NaCl, 2.7 mM KCl, 10 mM Na₂HPO₄, 1.8 mM KH₂PO₄) were purchased from Sigma-Aldrich. Concentric microdialysis probes (280 μm o.d., 4 mm long) were constructed with hollow fiber dialysis membrane (Spectra-Por RC Hollow Fiber, MWCO: 13,000, 160 µm i.d., Spectrum Laboratories, Inc., Rancho Dominguez, CA) and fused silica outlet lines (150 μm o.d., 75 μm i.d., Polymicro Technologies, Phoenix, AZ) as described elsewhere [40]. Perfusion solutions include 4% paraformaldehyde (electron Microscopy Sciences), in 0.1 M phosphate buffer pH 7.3 and a 0.1% solution of yellow-green fluorescent nanobeads as received (0.1 µm diameter, FluoSpheres® carboxylate-modified polystyrene microsphere suspensions (2% solids) in water plus 2 mM sodium azide, Molecular Probes, Inc., Eugene, OR) in PBS. Sucrose was obtained from Fisher (Fisher Scientific, Pittsburgh, PA).

Silicon (100) wafers (125 mm diameter, 650 µm thickness, 2 µm thermally grown silicon dioxide) used as the substrate material during probe fabrication, were purchased from Silicon Quest International, Santa Clara, CA. Chromium adhesion and gold electrode layers were deposited on the

silicon wafers using chromium coated tungsten rods (Kurt J. Lesker Company, Clairton, PA) and the small pieces of gold (99.99%) placed in a molybdenum boat (Kurt J. Lesker Company, Pittsburg, PA). Aluminum pellets (99.99%, from Alfa Aesar, Ward Hill, MA) in a molybdenum boat were used to deposit the sacrificial layer. The chromium mask was designed in house using AutoCAD® 2017 and manufactured by Advance Reproduction Corporation, North Andover, MA. The S1805 positive photoresist (Rohm and Haas Electronic Materials LLC, Marlborough, MA), AZ 300 MIF developer (AZ Electronic Materials, Somerville, gold etchant (Transene, GE8148) and chromium etchant (HTA Enterprise, CEP200) were used to pattern electrodes. SU-8 3050, SU-8 2000, adhesion promoter (Omnicoat), and SU-8 developer were obtained from MicroChem (Newton, MA).

Fabrication of the Electrodes

The design of the electrodes, insulation layer and substrate shape are shown in Fig. 1. To pattern the electrodes and insulate them on the SU-8 probe, conventional photolithography was employed. The bare wafer was first rinsed thoroughly with a sequence of acetone, IPA, and water, and then dehydrated in a convection oven (Blue M Convection oven, Baker Furnace Inc., Brea, CA) at 200 °C for 20 min. Then, the silicon wafers were coated with an Al layer (~50 nm) by thermal evaporation (Edwards 306 Auto thermal evaporator, Edwards Electronics, Clinton, MA). This acted as a sacrificial layer that was dissolved to release the probes from the wafer in the last step. Omnicoat (MicroChem, Newton, MA) was used in an attempt to improve adhesion to the Al layer, but it caused SU-8 to lift off in an unexpected manner especially at baking and development steps. Hexamethyldisilazane (HMDS) did not improve adhesion, either. Therefore, SU-8 was spin-coated (Eaton spin coater, Excel TeQ, Boston, MA) onto the aluminum-coated wafer directly and without an adhesion promoter.

The SU-8 layer (SU-8 3050) was spin coated onto the rinsed and dried Al-coated carrier wafer at 2500 rpm. It was observed that pouring SU-8 directly out of the bottle (versus dispensing it through a syringe) minimizes trapping of air bubbles. These bubbles make the surface of the SU-8 non-uniform and lead to imperfect contact of the chromium photomask with the wafer. Solvent was removed by pre-exposure baking on a hotplate at 95°C. Use of a hotplate instead of an oven was critical at this stage. In an oven, a crust forms on the surface of the SU-8 layer due to heating from the outside, inward, which traps solvent inside and prevents it from evaporating. The manufacturer suggests ramping the temperature of the hotplate up and down. Without these ramps, the internal stress within the SU-8 film causes the SU-8 to exhibit a curl after the probe release step. However, there is a tradeoff between the ramps and the bake time. Long ramps mean increased time on the hotplate, which leads to SU-8 sheets that are not photo-definable. In the cases described below, the wafer was pre-baked with a 70 °C/h ramp from 65 to 95 °C. The wafer was held at 95 °C for 20 min and then the cool-down ramp was achieved by turning the hotplate off and letting the wafer cool to 55 °C, which took about 1 h.

For the thick SU-8, a ring of polymer with an increased height that forms around the rim of the wafer, called an edge bead, can prevent the mask from making sufficient contact with the wafer, and substantially deteriorate the spatial resolution of the transferred pattern. In the literature, there are multiple ways of addressing edge bead issues of photoresists. For this study, we removed them by creating an edge bead mask, where the blank mask was modified to be dark field around the edges of the wafer (Fig. 2(a)). Thus, when the rest of the SU-8 substrate layer was cross linked by exposure through this mask, the edge bead was unaffected and could be dissolved away in the subsequent developer solution. The exposure under the edge bead mask was performed right after the pre-bake step with a dosage of 300 mJ/cm² using a Karl Suss MA150 mask aligner (Suss Microtec, Garching, Germany). A

short post developer bake was performed by moving the wafer from a 45 °C hotplate to a 65 °C hotplate (keeping the wafer on each hotplate for 1 min) to the 95 °C hotplate for 5 min and then repeating the process in reverse order.

Next, the wafer was strongly agitated in the SU-8 developer solution for 20 min to dissolve the edge beads. The wafer was subsequently rinsed with IPA and inspected. If the presence of white residue over the un-crosslinked areas was observed, further development was performed to remove this uncrosslinked SU-8. To dry the wafer, it was put in the spin coater and spun at 1000 rpm. Then, 50 mL of IPA were dispensed through the hole in the lid of the spin coater onto the spinning wafer, once the dispensing of IPA finished, the spinner was allowed to ramp down to zero rpm over 10 s. The wafers were placed in an oxygen plasma cleaner (Model: APE 110, LFE plasma systems, Clinton, MA) at 60 sccm oxygen flow, 60 W for 2 min. This step is recommended because it also roughens the surface of the SU-8 so that the adhesion of the subsequent metal layers is improved [41]. A Cr layer (~8 nm) and Au layer (~100 nm) were thermally evaporated onto the SU-8-coated substrate. Then, positive photoresist was spin coated at 3000 rpm for 30 s and baked on a hotplate at 65 °C for 30 s. See Fig. 2(b).

The electrodes, leads and contact pads were then patterned into the resulting metal film using conventional photolithography methods. See Fig. 3(a)-3(c). In short, the positive resist was exposed through the electrode chrome mask at a 70 mJ/cm² exposure rate (Fig. 3(a)). The wafer was developed for 45 s in the AZ-300 MIF solution and the metals were etched using their respective wet etchant solutions (15 s for gold and 5 s for Cr) (Fig 3(b)). The protective photoresist layer was then flood exposed for 1 min and developed for 2 min, and the wafer was cleaned from residual photoresist by using a plasma cleaner at 60 sccm oxygen flow, 40 W for 1 min.

A thin SU-8 layer (SU-8 2002) was then spin coated at 100 rpm for 30 s, baked on a 65 °C hotplate for 30 s and moved to the 95 °C hotplate for 2 min. The wafer was allowed to cool for 20 min after being taken off the hotplate. The wafer was then patterned using the insulation layer mask at 275 mJ/cm². The wafer was post baked for 2 min on a 65 °C hotplate and developed in the SU-8 developer solution for 1 min (Fig 3(c)). This step created openings through the insulator layer over the array electrodes and over the contact pads.

Shaping of the Probes

The shapes of the individual probes were produced by cutting a trench through the SU-8 layers of the patterned and insulated wafers, which allowed access of etchant to the underlying Al sacrificial layer (Fig. 3(c)). A 355 nm Nd:YAG 34 laser micromachiner (E-355H-ATHI-O system, Oxford lasers, UK) was used with 2 passes at a pulse fluence of 29 J cm⁻² and pulse spacing of 3 µm to minimize burning the material. The Al layer was subsequently etched overnight in a static solution of concentrated KOH in a chemical release step. The probes could then be lifted individually from the substrate (Fig. 3(d)).

Scanning electron microscopy (SEM) was performed by a Philips XL30 ESEM with 1000x magnification, using a secondary electron detector, 10 kV acceleration voltage and at a pressure of 0.4 to 1.1 Torr.

Electrochemical Studies

Electrochemical experiments were performed with a bipotentiostat (CHI 750A, 760E and 760B, CH Instruments, Austin, TX), equipped with a Faraday cage and a picoamp booster (CH Instruments, Austin, TX). The reference electrode was AglAgCl in saturated KCl and the working electrode was a Pt flag. A Molex zero insertion force (ZIF) edge connector with 1.00 mm pitch and 9 circuits (part number 52610-

0972) was used to connect the device to the bipotentiostat. Because the edge connector is small and fragile, it was soldered onto a circuit board (OSHPark company) and the board was connected to the pin header leading to wires that could be clamped to the potentiostat's leads.

Electrochemical characterization of individual electrodes (Fig. S1) on the probe was performed by cyclic voltammetry (CV) in a 1.02 mM solution of $[Fe(CN)_6]^{3-}$ and 0.1 M KCl. The potential was swept at 0.020 V/s from 0.550 V to -0.150 V and back to 0.550 V vs Ag|AgCl (saturated KCl).

Redox cycling involved activating five adjacent band electrodes in the array at a time, where the second and fourth were shorted together to serve as generators and the first, third, and fifth were shorted together to serve as collectors. CV was performed at the generators at 0.020 V/s, and the collectors were held at a constant potential equal to the starting potential of the CV at the generators. Before each redox cycling run, the CV response was recorded at the shorted generators, with the collectors at open circuit. For the solutions containing $[Fe(CN)_6]^{3-}$ in 0.1 M KCl, CV at 0.020 V/s was performed at the generators from 0.550 V to -0.150 V and back to 0.550 V vs AglAgCl (saturated KCl), while the collectors were held at a constant anodic potential of 0.550 V. Concentration studies were performed by spiking a solution of 0.10 M KCl in the electrochemical cell with different volumes of a stock solutions of 0.21 mM, 5.18 mM, or 9.94 mM $[Fe(CN)_6]^{3-}$ in 0.10 M KCl, to achieve consecutively higher concentrations of $[Fe(CN)_6]^{3-}$: 1.0 μ M, 2.0 μ M, 4.5 μ M, 13.0 μ M 20.4 μ M, 99.7 μ M, 226.5 μ M, 410.9 μ M, and 1.2 mM.

For solutions containing dopamine in artificial cerebral spinal fluid (aCSF) (consisting of 100 mM NaCl, 5.0 mM KCl, 1.2 mM NaH₂PO₄, 5.0 mM NaHCO₃, 10 mM glucose, 2.5 mM HEPES, 1.2 mM MgSO₄, 1.0 mM CaCl₂ at 7.4 pH), CV at 0.020 V/s was performed at the generators from -0.100 to

0.500~V and back to -0.100~V vs Ag|AgCl (saturated KCl), while the collectors were held at a constant cathodic potential of -0.100~V. Concentration studies were performed by spiking a solution of aCSF in the electrochemical cell with different volumes from a freshly prepared stock solution of 0.52~mM dopamine in fresh aCSF to achieve consecutively higher concentrations of dopamine: $2.2~\mu M$, $3.6~\mu M$, $10.7~\mu M$ and $49.1~\mu M$. To minimize oxidation of catecholamines by oxygen, the Faraday cage and all the solutions containing aCSF and dopamine were purged with argon prior to and during the experiments. The probe was kept dry in an enclosed container before the initial electrochemical studies involving $[Fe(CN)_6]^{3-}$. The probe was then stored in water between the initial studies with the model compound and subsequent dopamine studies.

To measure plateau current from CV responses, a tangent to the background current early in the forward sweep was first extrapolated through plateau current region. Then, the difference was taken between the plateau current (the current at -0.100 V for $[Fe(CN)_6]^{3-}$ and 0.400 V for dopamine) and the value of the extrapolated background current at that same potential.

Assessment of Tissue Damage

All procedures involving animals were approved by the Institutional Animal Care and Use Committee of the University of Pittsburgh. Male Sprague—Dawley rats (250-350 g body weight, Charles River, Raleigh, NC) were anesthetized with isoflurane (5% initially, 2.5% for maintenance) and maintained at a body temperature of 37 °C using a heat blanket (Harvard Apparatus, Holliston, MA). The anesthetized rat was placed in a stereotaxic frame (David Kopf, Tujunga, CA) and the dura mater was exposed by craniotomy and removed to allow device (listed below) in to the dorsal striatum at AP +1.0 mm from

bregma, ML +3.8 mm from midline, and DV 4.8 mm below the brain surface. The rats remained anesthetized throughout the following procedures.

The devices used during this work were a microdialysis probe (280 μ m in diameter with a 4-mm active length [42]), a carbon fiber electrode (7 μ m in diameter with a 350- μ m active length) and a "blank SU-8 probe" (SU-8 substrate with non-patterned Cr and Au layers on top). These were implanted individually into the striatum of different rats. The SU-8 probe was removed after 1 hr, while the microdialysis probe and carbon fiber were removed after 4 hr. While implanted, the microdialysis probe was perfused with an aCSF solution at 1.67 μ L/min and the carbon fiber underwent FSCV-style voltage scanning [15].

Following device explantation, the tissue was fixed by transcardial perfusion with 200 mL phosphate buffer saline (1x PBS: 155 mM NaCl, 100 mM phosphate, pH 7.40) followed by 250 mL of 4 % paraformaldehyde (PFA) and 50 mL of 0.1 % fluorescent nanobeads (Invitrogen, Eugene, OR). The brain was removed and then post fixed for 2 h in 4 % PFA, soaked overnight in 30 % sucrose at 4 °C for cryoprotection. The brain was removed from sucrose solution and frozen by dipping in liquid nitrogencooled 2-methylbutane and stored at -80 °C until sliced. Horizontal tissue sections (perpendicular to the insertion track) were cut at 30 µm using a cryostat. Sections were covered with gelvatol (Electron Microscopy Sciences) mounting medium (polyvinyl alcohol, glycerol, Tris buffer pH 8.5, and sodium azide in water) and covered with a cover slip Fluorescence microscopy was performed with a 20× objective (Olympus BX61, Olympus; Melville, NY) and filter sets (Laser: Diode laser: 488nm) as appropriate for the nanobeads and IgG-CY3 (Chroma Technology, Rockingham, VT). The center of the probe track in each slice was positioned so that it was in the middle of the microscope viewing area.

Image processing was performed with Metamorph/Fluor 7.1 software (Universal Imaging Corporation; Molecular Devices).

Results and Discussion

Probe design and rationale

The probe was carefully designed based on several criteria. A photo of the completed device and SEM image of its tip are shown in Fig. 4. The shape of the tip was designed to come to a point, because it is conventionally accepted that increased sharpness helps improve insertion in biological tissue [43]. A schematic with all of the dimensions is in Fig. 1(a). Critical for in vivo studies are the dimensions of the shank. The length is 6 mm for *in vivo* dopamine measurement in the dorsal striatum, located about 4 mm below the brain surface. The width is 100 µm, which is broad enough to construct an array of microband electrodes with conventional photolithography and leave sufficient space flanking the outermost electrodes for shaping by laser micromachining. This width is also narrow enough to minimize tissue damage. It is known after inserting a 280-µm diameter microdialysis probe that widespread tissue damage and glial response can extend to 300 µm away [10]. However, penetration injury surrounding a 7-µm diameter carbon fiber electrode is essentially non-detectable [44]), which allows carbon fiber electrodes to be placed in close proximity to dopamine terminals [10].

The electrode design on the probe consists of nine parallel, individually addressable bands, each of 4 µm width (measured 3.8 µm after fabrication), with 4 µm gaps (measured 4.2 µm after fabrication) between them (Fig. 1(b)). These dimensions were chosen because they are easily resolved with conventional photolithography and electrochemical results can be compared with our prior redox cycling studies on arrays having the same width and gap measurements [4, 45]. A thin insulating layer of SU-8

covers the leads on the probe and leaves an opening of $76 \times 100~\mu m^2$ near the tip that exposes the band electrodes for electrochemical analysis. This opening also defines the electroactive length of the electrodes to 100- μm , which is similar to the length of conventional carbon fiber electrodes used for in vivo measurements in the striatum [15, 46]. The exposed contact pads allow for connection to the bipotentiostat through the edge connector.

Characterization by Cyclic Voltammetry of Individual Electrodes with a Model Compound

CV in a 1.02 mM solution of the model compound $[Fe(CN)_6]^{3-}$ and 0.1 M KCl was used to characterize the probe electrodes. Sigmoidally shaped responses for each of the nine electrodes are shown in Fig. S1 of Supplementary Information. The scan rate is slow enough to achieve an average quasi-steady state plateau current, i_{qss} , at 0 mV vs. Ag/AgCl (sat'd KCl) of -4.72 ± 0.13 nA for electrodes 1 through 8 (± one standard deviation). The magnitude of electrode 9's plateau current is only -2.95 nA. This is due to partial coverage of that electrode by the nearby top insulation layer.

The i_{gss} from a potential step experiment with a microband electrode is expressed by Eq. 1 [47],

$$i_{qss} = \frac{2\pi nFlC^*D}{\ln(\frac{64Dt}{w^2})} \tag{1}$$

where w is the electrode width (3.8 µm), l is the electrode length (100 µm), C*is the bulk and initial concentration of the oxidized form of the redox species (1.02 x 10^{-6} mol/cm³), n is the number of moles of electrons needed to reduce a mole of $[Fe(CN)_6]^{3-}$ (n = 1), F is the Faraday constant (96485.3 C/mol e⁻), D is the diffusion coefficient for $[Fe(CN)_6]^{3-}$ (7.20 x 10^{-6} cm²/s at 25 °C) [48] and t is the time after stepping to a diffusion-limited potential. For a slow scan rate, the plateau current of the CV response at a microband electrode can be estimated by this equation. Here, t is taken as the time for the CV to sweep

from $E_{1/2}$ to 0 V, where the plateau current was measured, t = 0.25 V / 0.02 V/s = 12.5 s. With these parameters, Eq. 1 yields $i_{qss} = -4.53$ nA, which is outside the 95% confidence interval of the experimental data. A plausible explanation comes from the uncertainty in estimating t for Eq. 1 from a CV response and the derivation of Eq. 1, where the current approximates a two-dimensional diffusion and therefore ignores end effect contributions. It has been suggested that the length-to-width ratio should be 50 for end effects to be negligible [49]. Our length-to-width ratio is only 25. The five adjacent electrodes that had the most similar CV responses (3 through 7) were then selected to perform the redox cycling experiments. Throughout this paper, the electrodes in the array that are activated for the redox cycling studies are referred to as the "first" through "fifth" electrodes, to facilitate discussion.

Redox Cycling and Calibration Curves for a Model Compound

To determine the performance of redox cycling at the array on the probe, five adjacent electrodes were activated in solutions of different concentrations of $[Fe(CN)_6]^{3-}$ in 0.1 M KCl. The second and fourth electrodes were shorted together and served as generator electrodes. The first, third, and fifth electrodes were shorted together and served as collector electrodes. CV was used at the generator electrodes, instead of a potential step, given its diagnostic power to view electrochemistry throughout a potential range rather than at a single value. The potential was initially swept cathodically (between 0.550 and -0.150 V), at 0.020 V/s to ensure a steady state redox cycling response across the 4- μ m gap, with the collectors held at a constant anodic potential of 0.550 V which is sufficient to oxidize cathodically-generated Fe(CN)₆⁴⁻ and increasing the flux of Fe(CN)₆³⁻. The electrochemical responses are shown in Fig. 5.

At first, CV was performed at the shorted generators, i_{GEN}, while the collector electrodes were left at open potential and are sigmoidally-shaped (Fig. 5 (c1) and (c2)), similar to the single electrode

responses (Fig. S1 in the Supplementary Information). The solution containing 1.02 mM [Fe(CN)₆]³⁻ has a cathodic plateau current of -7.63 nA, only 1.6 times (not 2 times) the average of the individual electrode plateau currents, because of shielding effects, when diffusion layers of the closely spaced, similarly biased electrodes overlap. To approximate the diffusion length in one dimension, we use $x = \sqrt{2Dt}$ where x is the root mean squared distance that molecules diffuse in time t [47]. For D = 7.20 × 10⁻⁶ cm²/s and t = 12.5 s, x = 137 µm, which extends well beyond the gap of 12 µm between the generators and confirms that shielding takes place.

The experiment was then repeated with the collector electrodes also turned on and held at a constant oxidizing potential to achieve redox cycling. The current responses at the generators, $i_{GEN/RC}$ are shown in Figs. 5 (b1) and (b2), and those at the collectors, $i_{COLL/RC}$, are shown in Figs. 5 (a1) and (a2). During CV, as the potential at the generators nears the half-wave potential of the redox species, $E_{1/2}$, the cathodic current grows as more $[Fe(CN)_6]^{3-}$ species reduce there. Meanwhile, the anodic current at the collector electrodes increases as more $[Fe(CN)_6]^{4-}$ species arrive from the generator electrode and oxidize back to the starting form, $[Fe(CN)_6]^{3-}$. In the return sweep of the generators, at potentials more positive of $E_{1/2}$ the production of $[Fe(CN)_6]^{4-}$ diminishes and the magnitude of the collector current decreases correspondingly.

Linear calibration curves for the absolute values of background-subtracted plateau currents of i_{GEN} , $i_{GEN/RC}$, and $i_{COLL/RC}$ at 0.400 V were produced for a series of concentrations of $[Fe(CN)_6]^{3-}$ and yielded the following slopes (calibration sensitivities): 0.0064 ± 0.0002 , 0.0112 ± 0.001 , and 0.00777 ± 0.0007 nA/ μ M, respectively. See Fig. 6. That for $i_{GEN/RC}$ is greater than for i_{GEN} by a factor of 1.76 \pm 0.06, because of the enhanced concentration gradient established by re-oxidization of the reduced form at the neighboring collector electrodes. This ratio is called the amplification factor:

$$A_{f} = \frac{i_{GEN/RC}}{i_{GEN}} \tag{2}$$

The calibration sensitivity of the anodic $i_{COLL/RC}$ is greater than that for the cathodic i_{GEN} because of the concentration gradient established by reduction of the oxidized form at the generator electrodes. The ratio of the slopes of $i_{COLL/RC}$ and $i_{GEN/RC}$ is 69.15 $\pm 0.73\%$. This quantity represents the percent collection efficiency, $\%C_e$, which is a measure of the relative number of molecules recycled between generator and collector electrodes:

$$\%C_{e} = 100\% \left(\frac{i_{COLL/RC}}{i_{GEN/RC}}\right)$$
 (3)

The amplification factor and collection efficiency depend on the relative widths and numbers of generators to collectors and the size of the gaps between them. Comparisons of our results can be made to those obtained with similar array designs reported previously. The electrode lengths and model compounds are different but should not affect A_f and C_e substantially. One is by Aggarwal et. al. (2 mm-long electrodes, but with the same electrode widths, gaps and configuration as the work described here), who report an A_f of 1.4 and C_e of 60.6% for 5.0 mM Ru(NH₃)₆³⁺ [5]. Another is the Si₃N₄ probe, which exhibited an A_f of 1.5 and 2.0 and C_e of 54.0 and 65.0% for 1 mM Ru(NH₃)₆³⁺ on the 2-pair and 3-pair IDA (250- μ m long and 3- μ m wide electrodes with 2- μ m gaps), respectively [21].

The experimental calibration sensitivity for $i_{GEN/RC}$ is a factor of 0.67 at the Aggarwal microband electrode array [5] compared to the theoretical slope (0.016 nA/ μ M) of the diffusion limited current, i_{lim} , vs. C* using Eq. 4 [50] for redox cycling,

$$i_{lim} = mlnFC^*D \left[0.637 \ln(2.55(1 + \frac{w}{w_g}) - (\frac{0.19}{(1 + \frac{w}{w_g})^2})) \right].$$
 (4)

Here, i_{lim} is the same at the generators and collectors, m is number of generators and collectors (m = 2.5, accounting for a total of five electrodes used in redox cycling experiments in this paper), w is the width

of an individual electrode, where generator and collector widths are equal ($w = 3.8 \, \mu m$) and w_g is the width of the gap between anodes and cathodes ($w_g = 4.2 \, \mu m$). The value we use for D ($6.93 \times 10^{-6} \, \text{cm}^2/\text{s}$) in Eq. 4 is the average of Do and D_R for potassium ferri- and ferrocyanide in 0.1 M KCl at 25 °C reported by Konopka et al. [48]. This is because the expression of Eq. 4 assumes that the diffusion coefficients of reduced and oxidized forms are the same [50]. Eq. 4 makes several assumptions: (1) the array comprises of so many electrodes that the edge effects of the outermost electrodes are negligible; (2) the length-to-width ratio for each electrode is so large that end effects can be ignored; (3) the diffusion coefficients of reduced and oxidized forms of redox species are the same; (4) the system is at steady state; and (5) $w > 0.18 \, w_g$. The experimental slope is a factor of 0.46 of that predicted by Eq. 4. This can be explained at least partially by the fact that the first two assumptions do not apply to our probe design. (It has been shown previously that with increasing numbers of pairs of generators and collectors that $|i_{COLL/RC}|$ approaches that of $|i_{GEN/RC}|$ [51, 52].)

Detection limits for $[Fe(CN)_6]^{3-}$ were 2.19 μ M, 1.25 μ M and 2.08 μ M, for i_{GEN} , $i_{GEN/RC}$, and $i_{COLL/RC}$, respectively. These were determined by the quotient of three times the standard deviation of the background current and the slope of the calibration curve. The background was obtained by performing CV in the blank KCl solution (N = 4). For the most part, these detection limits are higher than detection limits using redox cycling reported elsewhere but for different model compounds (e.g. 10.0 nM $[Ru(NH_3)_6]^{3+}$ [53] and 20 nM of $[Ru(NH_3)_6]^{3+}$ [21]). This is likely due to the fact that our probe has at least one or more of the following: shorter electrodes, fewer pairs of them and wider gaps.

Redox Cycling and Calibration Curves for Dopamine

Redox cycling of dopamine in aCSF in vitro and at the same probe electrodes as for the model compound was performed to demonstrate an application to an analyte of biological significance and a target for

future *in vivo* studies. The potential was swept between -0.100 V to 0.500 V at 0.020 V/s to oxidize the dopamine to the o-quinone, with the collectors held at a constant potential of -0.100 V to reduce the o-quinone form back to dopamine. The redox cycling responses are shown in Fig. 7. As in the ferricyanide solutions, the generator and collector electrode responses in the dopamine solutions are sigmoidal and similar in behavior, except in opposite directions of potential and current, because dopamine is in its reduced form. However, not all background currents align when overlaid for reasons that are unknown and are being investigated at this time.

Linear calibration curves for i_{GEN} , $i_{GEN/RC}$, and $i_{COLL/RC}$ were produced from the background-subtracted plateau currents at 0.4~V for a series of concentrations of dopamine and yielded the following calibration sensitivities: 0.021 ± 0.002 , 0.0420 ± 0.0004 , and $0.0328 \pm 0.0003~nA/\mu M$, respectively. See Fig. 8. As for $[Fe(CN)_6]^{3-}$, the calibration sensitivities for dopamine also increase in the order of i_{GEN} , $i_{COLL/RC}$ and $i_{GEN/RC}$. These values are higher by a factor of ~ 3.8 compared to those obtained for $[Fe(CN)_6]^{3-}$. The calibration sensitivity based on Eq. 4 (using $D = 7.5 \times 10^{-6}~cm^2/s$ [54]) is $0.035~nA/\mu M$. The expected increase is only 2.2 times that for $[Fe(CN)_6]^{3-}$, which should result from an increase in n from 1 to 2 and a slightly larger diffusion coefficient for dopamine. The unexpectedly higher experimental response could be due to increasingly clean electrode surfaces and hydration of SU-8 [55] over extended use and storage in aqueous solution between the $[Fe(CN)_6]^{3-}$ and dopamine studies. (More studies would be needed to understand this effect).

The amplification factor for dopamine for redox cycling at the probe's array using five electrodes is 2.01 ± 0.16 , obtained from the ratio of the slopes of calibration curves for $i_{GEN/RC}$ and i_{GEN} . The percent collection efficiency for dopamine during redox cycling is $78 \pm 1\%$, obtained from the ratio of the slopes for $i_{GEN/RC}$ and $i_{GEN/RC}$. These numbers are only slightly higher, by 1.1 times, than those obtained for

the model compound, because it is the electrode array geometries that contribute to these numbers, and that little to no effect is expected on Af and Ce% of enhancement to the electroactivity of the electrodes (assuming all electrodes are similarly enhanced).

The calculated detection limits for dopamine with this probe are $1.94~\mu M$, $1.08~\mu M$ and $5.66~\mu M$ for $i_{GEN, i_{GEN/RC,}}$ and $i_{COLL/RC}$, respectively. The insertable Si_3N_4 probe with IDA electrodes has reported detection limits of $1.0~\mu M$ of dopamine at the collector electrode at a 5-pair IDA [21], consistent with our results. To our knowledge, a detection limit of 10~n M dopamine is the lowest value demonstrated by redox cycling, using the vertical-stacked, interdigitated microelectrode arrays [53]. However, that particular device is not suitable for *in vivo* measurements because of the large footprint with more and longer electrodes and narrower gaps compared to this work. The dopamine detection limits for FSCV and microdialysis are in the low-nanomolar range [15, 56, 57].

Insertion of probe and assessment of resulting tissue damage in rat brain

Fig. 9 shows fluorescence microscopy images of tissue sections from the dorsal striatum of rat brain where three different probes had been inserted and vascularization labeled by subsequent perfusion with fluorescent nanobeads. The white outlines indicate that of the probe traces in the tissue. The control image was obtained from the opposite hemisphere of the brain in which the SU-8 probe was inserted. In the case of the 7-μm carbon fiber, the track of the glass pipet encapsulating the carbon fiber was followed to the smallest visible extent. The track of the electrode itself is very hard to find under the microscope [44] and its size and shape can only be estimated, because the diameter of the electrode is so small [10]. As for the microdialysis probe, the tissue damage is substantial as can be seen by the absence of blood vessels around the probe's track. The SU-8 probe shows relatively low tissue damage as seen by the

presence of many blood vessels around the track. Note, the time differences of these devices in Fig. 9 is 4 h and 1 h. The dwelling time of each device is indicative of the timeframe typically used in brain tissue. For example, 4 h is a very common timescale for microdialysis probe implantation, although current literature cite up to 10 days of dwelling time [42, 58]. Damage to the tissue from the SU-8 probe is most similar to that of the carbon fiber microelectrode (Fig. 9 b and c). Regardless of these timeframes it is clear that the SU-8 probe offers the benefits of the smaller single carbon fiber electrodes but with the additional capabilities of multiple electrodes and redox cycling.

Conclusions

The studies here emphasize the fabrication of a flexible SU-8 probe with an array of individually-addressable microband electrodes and the preliminary results of their redox cycling behavior. The dimensions and shape are suitable for in vivo measurements. Because the electroactive tip occupies a volume of only about 1 µL, analysis in other kinds of ultrasmall samples of this size is possible. The electrode fabrication process was performed with modifications to established lithographical procedures, and the shape of the probe was accomplished by laser cutting through the SU-8 substrate and lift off by dissolving the metallic sacrificial layer. Tissue damage in rat dorsal striatum was minimal. Redox cycling produced predictable behavior and detection limits for a model compound and dopamine, comparable to other microelectrode arrays reported in the literature, accounting for the different designs and geometries, but most of which are not on tissue-insertable probes. A unique contribution is that the probe electrodes can be independently activated to allow for other electrochemical detection methodologies such as those that investigate following chemistry and kinetics or differentiate between analytes in mixtures based on these phenomena.

There remains a need to lower detection limits further to be able to measure physiologically relevant concentrations of dopamine [59]. To do so, narrowing the separation between generators and collectors while maintaining the same footprint can be considered. Achieving more electrode pairs with smaller gaps with stacked electrode arrays that also use the space perpendicular to the probe surface would further enhance signals. For an increasing number of electrodes to remain individually addressable, the need for more space for the leads should also be accounted for. Other possible modifications to improve detection limits include lengthening the electrodes, if larger detection regions are acceptable, and widening the probe shank to accommodate more electrodes, if tissue damage is tolerable. A more quantitative investigation of electrochemical performance of the array design, analysis of contributions of the SU-8 substrate and electrode imperfections toward electrochemical signal, and an assessment of alternative electrode dimensions that fit on the probe and improve detection limits will be reported elsewhere.

Supplementary Information

Supplementary information includes CV responses for individual electrodes in the ferricyanide solution.

Declarations

Conflicts of Interest

The authors declare that they have no conflicts of interest.

Ethics Approval

The University of Pittsburgh's Institutional Animal Care and Use Committee reviewed and approved all procedures involving animals.

Source of Biological Material

Male Sprague-Dawley rats were obtained from Charles River, Raleigh, NC.

Statement on Animal Welfare

All animal procedures were in compliance with USDA laboratory animal use regulations. Additionally, all procedures were approved by the Institutional Animal Care and Use Committee of the University of Pittsburgh, the location of the laboratory where all experiments involving animals took place

Acknowledgements

Research was supported partially through the National Institutes of Health (R01NS102725, R21NS109875) and the University of Pittsburgh Center for Biological Imaging (1S10RR028478-01), the Royal Society for an Industry Fellowship (J.V.M., INF/R1/180026) and the Centre for Doctoral Training in Diamond Science and Technology (EP/ L015315/1) with the Defense Science and Technology Laboratory (Dstl) (S.J.C.), the University of Arkansas's Women's Giving Circle, the National Science Foundation (CMI-1808286) and the Arkansas Biosciences Institute, the major research component of the Arkansas Tobacco Settlement Proceeds Act of 2000. MLM is also grateful for a Fulbright Dissertation Research Award. We thank Dr. Ben J. Jones for designing the table of contents graphic. We acknowledge Errol Porter for consultation on microelectrode fabrication and the High-Density Electronics Center for use of microfabrication facilities. Scanning electron microscopy images were obtained in the Arkansas Nano & Biomaterials Characterization Facility at the University of Arkansas. We are grateful to Dr. Jonathan Moldenhauer and Professor David Paul at the University of Arkansas for designing and providing the circuit board for mounting the edge connector.

References

- 1. Xu X, Zhang S, Chen H, Kong J. Integration of electrochemistry in micro-total analysis systems for biochemical assays: Recent developments. Talanta. 2009;80(1):8-18. doi: 10.1016/j.talanta.2009.06.039.
- 2. Niwa O. Electroanalytical chemistry with carbon film electrodes and micro and nano-structured carbon film-based electrodes. Bull Chem Soc Jpn. 2005;78(4):555-71. doi: 10.1246/bcsj.78.555.
- 3. Lowinsohn D, Peres HEM, Kosminsky L, Paixão TRLC, Ferreira TL, Ramirez-Fernandez FJ, et al. Design and fabrication of a microelectrode array for iodate quantification in small sample volumes. Sensor Actuat B-Chem. 2006;113(1):80-7. doi: https://doi.org/10.1016/j.snb.2005.02.024.
- 4. Hu M, Fritsch I. Redox cycling behavior of individual and binary mixtures of catecholamines at gold microband electrode arrays. J Anal Chem. 2015;87(4):2029-32.
- 5. Aggarwal A. Studies Toward the Development of a Microelectrode Array for Detection of Dopamine through Redox Cycling. Dissertation, University of Arkansas; 2011.
- 6. Niwa O. Electroanalysis with interdigitated array microelectrodes. Electroanalysis. 1995;7(7):606-13. doi: 10.1002/elan.1140070702.
- 7. Bard AJ, Crayston JA, Kittlesen GP, Varco Shea T, Wrighton MS. Digital simulation of the measured electrochemical response of reversible redox couples at microelectrode arrays: consequences arising from closely spaced ultramicroelectrodes. Anal Chem. 1986;58(11):2321-31. doi: 10.1021/ac00124a045.
- 8. Oleinick A, Zhu F, Yan J, Mao B, Svir I, Amatore C. Theoretical Investigation of Generator-Collector Microwell Arrays for Improving Electroanalytical Selectivity: Application to Selective Dopamine Detection in the Presence of Ascorbic Acid. Chem Phys Chem. 2013;14(9):1887-98. doi: 10.1002/cphc.201300134.
- 9. Seymour JP, Wu F, Wise KD, Yoon E. State-of-the-art MEMS and microsystem tools for brain research. Microsystems & Nanoengineering. 2017;3(1):16066. doi: 10.1038/micronano.2016.66.
- 10. Jaquins-Gerstl A, Michael AC. Comparison of the brain penetration injury associated with microdialysis and voltammetry. J Neurosci Meth. 2009;183(2):127-35. doi: 10.1016/j.jneumeth.2009.06.023.
- 11. Hong G, Lieber CM. Novel electrode technologies for neural recordings. Nat Neuroscience. 2019;20(6):330-45. doi: 10.1038/s41583-019-0140-6.

- 12. Dengler AK, McCarty GS. Microfabricated Microelectrode Sensor for Measuring Background and Slowly Changing Dopamine Concentrations. J Electroanal Chem. 2013;693:28-33. doi: 10.1016/j.jelechem.2013.01.022.
- 13. Zachek MK, Park J, Takmakov P, Wightman RM, McCarty GS. Microfabricated FSCV-compatible microelectrode array for real-time monitoring of heterogeneous dopamine release. Analyst. 2010;135(7):1556-63. doi: 10.1039/c0an00114g.
- 14. Roberts JG, Sombers LA. Fast-Scan Cyclic Voltammetry: Chemical Sensing in the Brain and Beyond. Anal Chem. 2018;90(1):490-504. doi: 10.1021/acs.analchem.7b04732.
- 15. Rodeberg NT, Sandberg SG, Johnson JA, Phillips PEM, Wightman RM. Hitchhiker's Guide to Voltammetry: Acute and Chronic Electrodes for in Vivo Fast-Scan Cyclic Voltammetry. ACS Chem Neurosci. 2017;8(2):221-34. doi: 10.1021/acschemneuro.6b00393.
- 16. Hunsberger HC, Setti SE, Heslin RT, Quintero JE, Gerhardt GA, Reed MN. Using enzyme-based biosensors to measure tonic and phasic glutamate in Alzheimer's mouse models. JoVE 2017(123):e55418.
- 17. Burmeister JJ, Pomerleau F, Huettl P, Gash CR, Werner CE, Bruno JP, et al. Ceramic-based multisite microelectrode arrays for simultaneous measures of choline and acetylcholine in CNS. Biosens Bioelectron. 2008;23(9):1382-9. doi: https://doi.org/10.1016/j.bios.2007.12.013.
- 18. Burmeister JJ, Price DA, Pomerleau F, Huettl P, Quintero JE, Gerhardt GA. Challenges of simultaneous measurements of brain extracellular GABA and glutamate in vivo using enzyme-coated microelectrode arrays. 2020(1872-678X (Electronic)).
- 19. Zachek MK, Takmakov P, Park J, Wightman RM, McCarty GS. Simultaneous monitoring of dopamine concentration at spatially different brain locations in vivo. Biosens Bioelectron. 2010;25(5):1179-85. doi: 10.1016/j.bios.2009.10.008.
- 20. Ngernsutivorakul T, White TS, Kennedy RT. Microfabricated Probes for Studying Brain Chemistry. Chem Phys Chem. 2018;19(10):1128.
- 21. Xi Y. Interdigitated array electrode microprobe: Design, fabrication and characterization. University of Arkansas; 2005.
- 22. Cao Q, Puthongkham P, Venton BJ. Review: new insights into optimizing chemical and 3D surface structures of carbon electrodes for neurotransmitter detection. Anal Methods-UK. 2019;11(3):247-61. doi: 10.1039/C8AY02472C.
- 23. Atcherley CW, Laude ND, Parent KL, Heien ML. Fast-scan controlled-adsorption voltammetry for the quantification of absolute concentrations and adsorption dynamics. Langmuir. 2013;29(48):14885-92.

- 24. Taylor IM, Patel NA, Freedman NC, Castagnola E, Cui XT. Direct in vivo electrochemical detection of resting dopamine using Poly (3, 4-ethylenedioxythiophene)/Carbon Nanotube functionalized microelectrodes. Anal Chem. 2019;91(20):12917-27.
- 25. Pathirathna P, Balla RJ, Amemiya S. Nanogap-Based Electrochemical Measurements at Double-Carbon-Fiber Ultramicroelectrodes. Anal Chem. 2018;90(20):11746-50. doi: 10.1021/acs.analchem.8b02987.
- 26. Hu M, Fritsch I. Application of electrochemical redox cycling: toward differentiation of dopamine and norepinephrine. Anal Chem. 2016;88(11):5574-8.
- 27. HajjHassan M, Chodavarapu V, Musallam S. NeuroMEMS: Neural Probe Microtechnologies. Sensors. 2008;8(10):6704-26. doi: 10.3390/s8106704.
- 28. Sreenivas G, Ang SS, Fritsch I, Brown WD, Gerhardt GA, Woodward DJ. Fabrication and characterization of sputtered-carbon microelectrode arrays. Anal Chem. 1996;68(11):1858-64.
- 29. Metallo C, White RD, Trimmer BA. Flexible parylene-based microelectrode arrays for high resolution EMG recordings in freely moving small animals. J Neurosci Meth. 2011;195(2):176-84.
- 30. Zhuolin Xiang S-CY, Ning Xue, Tao Sun. Ultra-thin flexible polyimide neural probe embedded in dissolvable maltose-coated microneedle. J Micromech Microeng. 2014;24:11-20.
- 31. Huang S-H, Lin S-P, Chen J-JJ. In vitro and in vivo characterization of SU-8 flexible neuroprobe: From mechanical properties to electrophysiological recording. Sensor Actuat A-Phys. 2014;216:257-65. doi: https://doi.org/10.1016/j.sna.2014.06.005.
- 32. Takeuchi S, Ziegler D, Yoshida Y, Mabuchi K, Suzuki T. Parylene flexible neural probes integrated with microfluidic channels. Lab Chip. 2005;5(5):519-23.
- 33. Keekeun Lee JH, Ryan Clement. Biocompatible benzyclobutene (BCB)-based neural implants with micro-fluidic channel. Biosens Bioelectron. 2004;20:404-7.
- 34. A. H. A. Malavazi JABG, R. J. M. Covolan, R. R. Panepucci. Design and microfabrication methodology of Su-8 based neural probes XXIV Congresso Brasileiro de Engenharia Biomédica. 2014:2850-3.
- 35. Nemani KV, Moodie KL, Brennick JB, Su A, Gimi B. In vitro and in vivo evaluation of SU-8 biocompatibility. Mater Sci Eng. 2013;33(7):4453-9. doi: https://doi.org/10.1016/j.msec.2013.07.001.
- 36. Read TL, Cobb SJ, Macpherson JV. An sp2 Patterned Boron Doped Diamond Electrode for the Simultaneous Detection of Dissolved Oxygen and pH. Sensors. 2019;4(3):756-63. doi: 10.1021/acssensors.9b00137.

- 37. Li A, Chan SH, Nguyen N-T. A laser-micromachined polymeric membraneless fuel cell. J Micromech Microeng. 2007;17(6):1107-13. doi: 10.1088/0960-1317/17/6/002.
- 38. Ghantasala MK, Hayes JP, Harvey EC, Sood DK. Patterning, electroplating and removal of SU-8 moulds by excimer laser micromachining. J Micromech Microeng. 2001;11(2):133-9. doi: 10.1088/0960-1317/11/2/308.
- 39. Green RA, Ordonez JS, Schuettler M, Poole-Warren LA, Lovell NH, Suaning GJ. Cytotoxicity of implantable microelectrode arrays produced by laser micromachining. Biomaterials. 2010;31(5):886-93. doi: https://doi.org/10.1016/j.biomaterials.2009.09.099.
- 40. Abercrombie ED, Keefe KA, DiFrischia DS, Zigmond MJ. Differential Effect of Stress on In Vivo Dopamine Release in Striatum, Nucleus Accumbens, and Medial Frontal Cortex. J Neurochem. 1989;52(5):1655-8. doi: 10.1111/j.1471-4159.1989.tb09224.x.
- 41. Matarèse BFE, Feyen PLC, Falco A, Benfenati F, Lugli P, deMello JC. Use of SU8 as a stable and biocompatible adhesion layer for gold bioelectrodes. Sci Rep-UK. 2018;8(1):5560-. doi: 10.1038/s41598-018-21755-6.
- 42. Nesbitt KM, Jaquins-Gerstl A, Skoda EM, Wipf P, Michael AC. Pharmacological mitigation of tissue damage during brain microdialysis. Anal Chem. 2013;85(17):8173-9. doi: 10.1021/ac401201x.
- 43. Hajj-Hassan M, Fayad R, Berro S, Chodavarapu VP, Musallam S. Implantation of Elongated Porous Silicon Neural Probe Array in Rat Cortex. Preprints. 2018.
- 44. Mitch Taylor I, Jaquins-Gerstl A, Sesack SR, Michael AC. Domain-dependent effects of DAT inhibition in the rat dorsal striatum. J Neurochem. 2012;122(2):283-94.
- 45. Aggarwal A, Hu M, Fritsch I. Detection of dopamine in the presence of excess ascorbic acid at physiological concentrations through redox cycling at an unmodified microelectrode array. Anal Bioanal Chem. 2013;405. doi: 10.1007/s00216-013-6738-z.
- 46. Venton BJ, Cao Q. Fundamentals of fast-scan cyclic voltammetry for dopamine detection. Analyst. 2020;145(4):1158-68. doi: 10.1039/C9AN01586H.
- 47. Bard AJ, Faulkner LR. Electrochemical methods: fundamentals and applications. 2nd ed. New York: Wiley; 2001.
- 48. Konopka SJ, McDuffie B. Diffusion coefficients of ferri- and ferrocyanide ions in aqueous media, using twin-electrode thin-layer electrochemistry. Anal Chem. 1970;42(14):1741-6. doi: 10.1021/ac50160a042.
- 49. Le Drogoff B, El Khakani MA, Silva PRM, Chaker M, Vijh AK. Effect of the Microelectrode Geometry on the Diffusion Behavior and the Electroanalytical Performance of Hg-Electroplated Iridium Microelectrode Arrays Intended for the Detection of Heavy Metal Traces. Electroanal.

- 2001;13(18):1491-6. doi: 10.1002/1521-4109(200112)13:18<1491::AID-ELAN1491>3.0.CO;2-Z.
- 50. Aoki K, Morita M, Niwa O, Tabei H. Quantitative analysis of reversible diffusion-controlled currents of redox soluble species at interdigitated array electrodes under steady-state conditions. J Electroanal Chem. 1988;256(2):269-82.
- 51. Niwa O, Morita M, Tabei H. Fabrication and characteristics of vertically separated interdigitated array electrodes. J Electroanal Chem. 1989;267(1):291-7. doi: https://doi.org/10.1016/0022-0728(89)80257-8.
- 52. Han D, Zaino Iii LP, Fu K, Bohn PW. Redox cycling in nanopore-confined recessed dual-ring electrode arrays. J Phys Chem C. 2016;120(37):20634-41.
- 53. Niwa O, Morita M, Tabei H. Highly sensitive and selective voltammetric detection of dopamine with vertically separated interdigitated array electrodes. Electroanalysis. 1991;3(3):163-8. doi: 10.1002/elan.1140030305.
- 54. Rice ME, Gerhardt GA, Hierl PM, Nagy G, Adams RN. Diffusion coefficients of neurotransmitters and their metabolites in brain extracellular fluid space. Neuroscience. 1985;15(3):891-902. doi: https://doi.org/10.1016/0306-4522(85)90087-9.
- 55. Wouters K, Puers R. Diffusing and swelling in SU-8: insight in material properties and processing. J Micromech Microeng. 2010;20(9):095013. doi: 10.1088/0960-1317/20/9/095013.
- 56. Gu H, Varner EL, Groskreutz SR, Michael AC, Weber SG. In vivo monitoring of dopamine by microdialysis with 1 min temporal resolution using online capillary liquid chromatography with electrochemical detection. Anal Chem. 2015;87(12):6088-94.
- 57. Yang H, Thompson AB, McIntosh BJ, Altieri SC, Andrews AM. Physiologically relevant changes in serotonin resolved by fast microdialysis. ACS Chem Neurosci. 2013;4(5):790-8.
- 58. Robbins EM, Jaquins-Gerstl A, Fine DF, Leong CL, Dixon CE, Wagner AK, et al. Extended (10-Day) Real-Time Monitoring by Dexamethasone-Enhanced Microdialysis in the Injured Rat Cortex. ACS Chem Neurosci. 2019;10(8):3521-31. doi: 10.1021/acschemneuro.9b00145.
- 59. Roberts JG, Lugo-Morales LZ, Loziuk PL, Sombers LA. Real-time chemical measurements of dopamine release in the brain. Methods Mol Biol. 2013;964:275-94. doi: 10.1007/978-1-62703-251-3 16.

Figure Captions

Fig. 1 AutoCAD drawings of the probe and microelectrode array. (a) The view of the entire probe. The blue outline defines the shape of the probe in the substrate layer (SU-8 3050), the red areas are the contact pads, leads, and electrodes in the metal layer. (b) Magnified view of the tip of the probe containing the electrode array. The green outline indicates the openings in the insulation layer (SU-8 2000) over the contact pads and electroactive region of the microband electrodes. Microband electrodes are assigned names of E1 to E9 from left to right with the paddle oriented to the top of the page

Fig. 2 Process flow of whole wafer (not to scale). (a) Blanket UV-exposure of the SU-8 substrate layer, excluding the edge bead, after spin-coating and pre-baking.. (b) Subsequent removal of the edge bead with developer, post-baking of the remaining substrate SU-8, followed by coating of wafer with Cr and Au metal layers, and spin coating and baking of positive photoresist

Fig. 3 Expanded view of the process of a single probe (not to scale) that follow steps in Fig. 2. (a) Defining an image of the electrodes in the photoresist through UV exposure through a chrome mask. (b) Developing unexposed positive resist followed by etching of Cr and Au metal layers. (c) Spin coating, pre-baking, UV-exposure through an aligned insulation chrome mask, development, and post-baking of insulating SU-8 layer, followed by laser cutting to create trenches through both SU-8 layers in a probe shape. (d) Releasing probes from substrate by dissolution of the underlying aluminum layer in a KOH solution

Fig. 4 (a) Photograph of a completed probe. (b) SEM image of the microarray on the tip of the SU-8 probe. A faint rectangular outline can be observed over the array, which is the edge of the top

layer of insulating SU-8 that borders an opening exposing the electrodes and defining their electroactive length

Fig. 5 Electrochemical responses for different concentrations of $K_3Fe(CN)_6$ in 0.10 M KCl during redox cycling when (a1) and (a2) collectors are held at +0.550 V vs. Ag|AgCl (saturated KCl) (anodic, positive current) and while (b1) and (b2) generators undergo CV at a scan rate of 0.020 V/s (cathodic, negative current), and without redox cycling when (c1) and (c2) generators undergo CV at a scan rate of 0.020 V/s and collectors are left at open circuit. Arrows indicate responses in the direction of increasing concentration. (a1), (b1) and (c1) overlay responses for concentrations of 1.0 μM, 2.0 μM, 4.5 μM, 13.0 μM, 20.4 μM, 49.4 μM, 99.7 μM, 226.5 μM and 410.9 μM and 1.2 mM. (a2), (b2) and (c2) are expanded views of (a1), (b1) and (c1), respectively, where the largest response corresponds to 99.7 μM

Fig. 6 Calibration curves of background-subtracted, plateau current (measured at 0.0 V) on increasing concentrations of K_3 Fe(CN)₆ for generators without redox cycling (green squares), and for generators (red circles) and collectors (blue diamonds) with redox cycling. The absolute value of current has been plotted for a simpler overlay. The least squares fit and corresponding R^2 values for curves for i_{GEN} , i_{GEN} , and $i_{GEN/RC}$ are: $y = (6.38 (\pm 0.22) \times 10^{-3} \text{ nA } \mu\text{M}^{-1}) \times + (0.11 (\pm 0.01) \text{ nA})$, $R^2 = 0.990$; $y = (1.12 (\pm 0.01) \times 10^{-2} \text{ nA } \mu\text{M}^{-1}) \times + (0.17 \pm 0.03 \text{ nA})$, $R^2 = 0.999$ and $y = (7.77 (\pm 0.07) \times 10^{-3} \text{ nA } \mu\text{M}^{-1}) \times + (0.14 \pm 0.03 \text{ nA})$, $R^2 = 0.999$; respectively. Inset shows calibration curve for concentrations below 50 μM

Fig. 7 Electrochemical responses in different concentrations of dopamine in aCSF without redox cycling for (a) generators at 0.020 V/s, and with redox cycling for (b) generators at 0.020 V/s and

(c) collectors held at -0.100 V vs. Ag|AgCl (saturated KCl). Arrows indicate responses in the direction of increasing concentration of dopamine: $2.2~\mu M$, $3.6~\mu M$, $10.7~\mu M$ and $49.1~\mu M$

Fig. 8 Calibration curve of background-subtracted, plateau current (measured at 0.4 V) on increasing concentrations of dopamine for generator without redox cycling (green diamonds), generator with redox cycling (red circles) and collector with redox cycling (blue squares).. The absolute value of current has been plotted for easier overlay. The least squares fit and corresponding R² values for curves for i_{GEN}, i_{GEN}, and i_{GEN/RC} are: $y = (2.09 (\pm 0.17) \times 10^{-2} \text{ nA} \, \mu\text{M}^{-1}) \times (4.71 (\pm 0.34) \times 10^{-2} \, \text{nA})$, R² = 0.975; $y = (4.20 (\pm 0.04) \times 10^{-2} \, \text{nA} \, \mu\text{M}^{-1}) \times (2.60 (\pm 0.94) \times 10^{-2} \, \text{nA})$, R² = 0.999; $y = (3.28 (\pm 0.03) \times 10^{-2} \, \text{nA} \, \mu\text{M}^{-1}) \times (1.74 (\pm 0.60) \times 10^{-2} \, \text{nA})$, R² = 0.999 respectively

Fig. 9 Fluorescence microscope images of tracks of an inserted probe. White outlines show the perimeter of the probe's track. The green streaks show blood vessels in the slice. The scale bar is the same for all images. (a) The control image was obtained from the opposite side of the brain in which the microelectrode array probe was inserted. (b) Track of the probe used for this study. (c) Track of a 5-μm diameter carbon fiber electrode. (d) Track of a typical 300-μm diameter microdialysis probe. In the control image, the round green outline is the cross section of a blood vessel

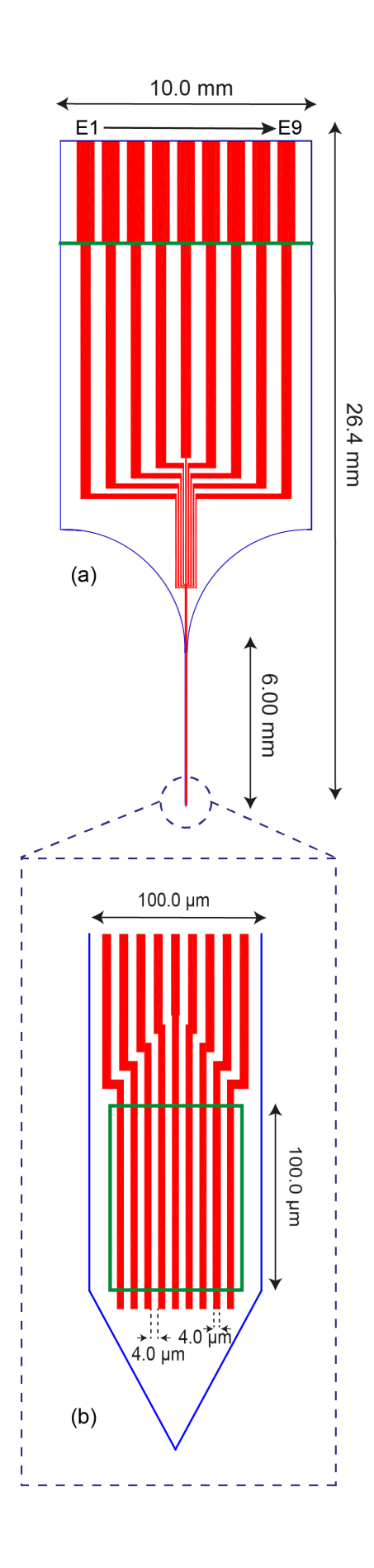


Figure 1

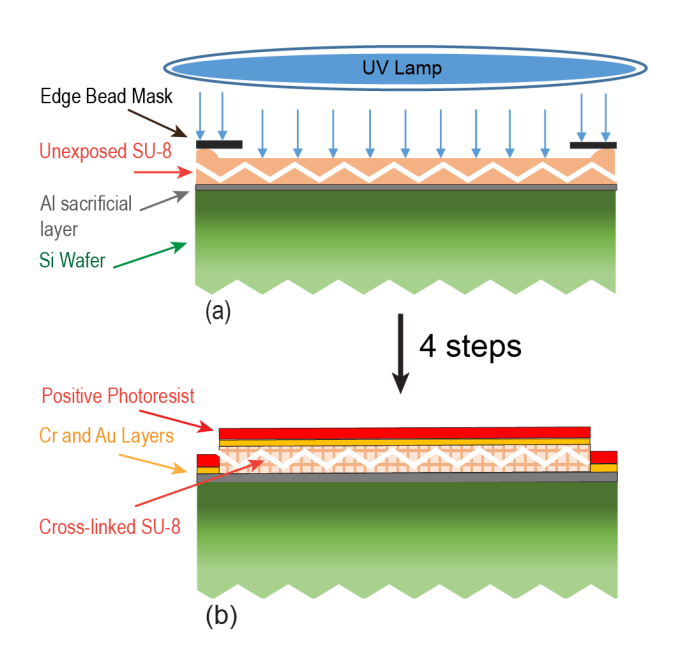


Figure 2

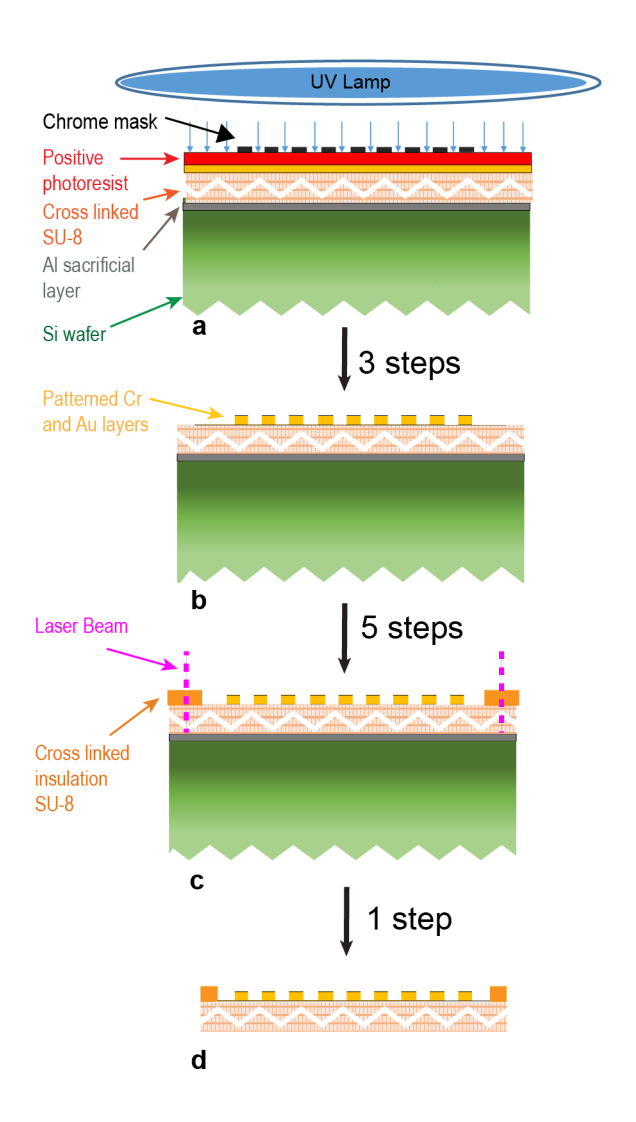


Figure 3

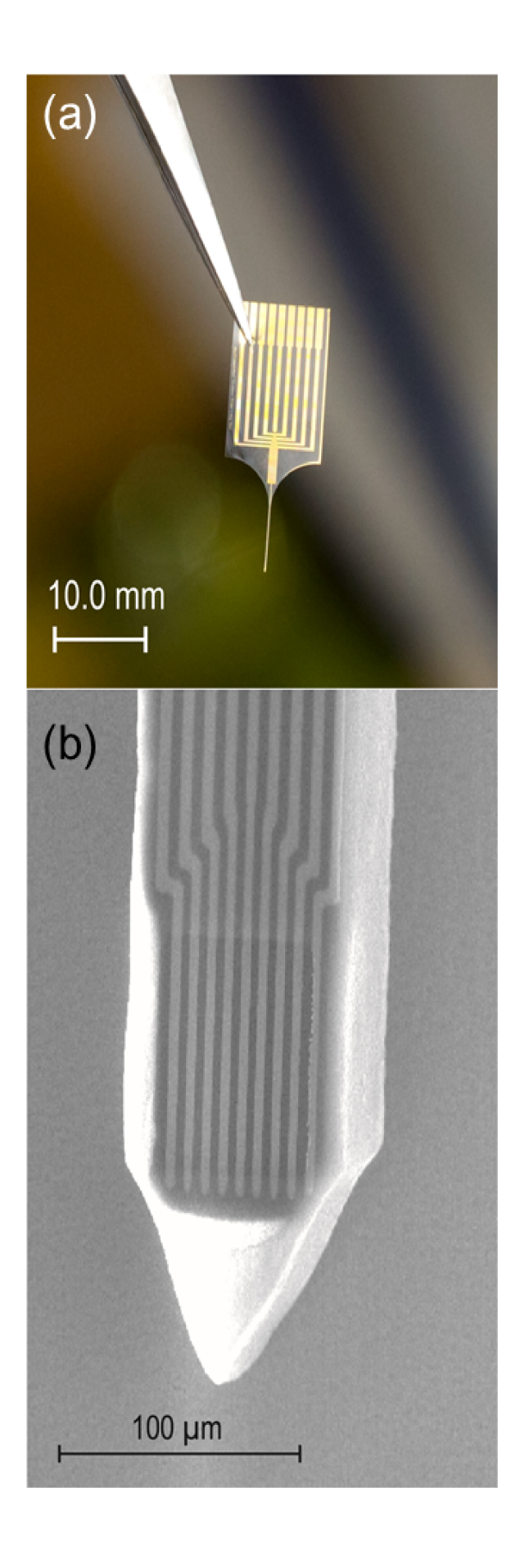


Figure 4

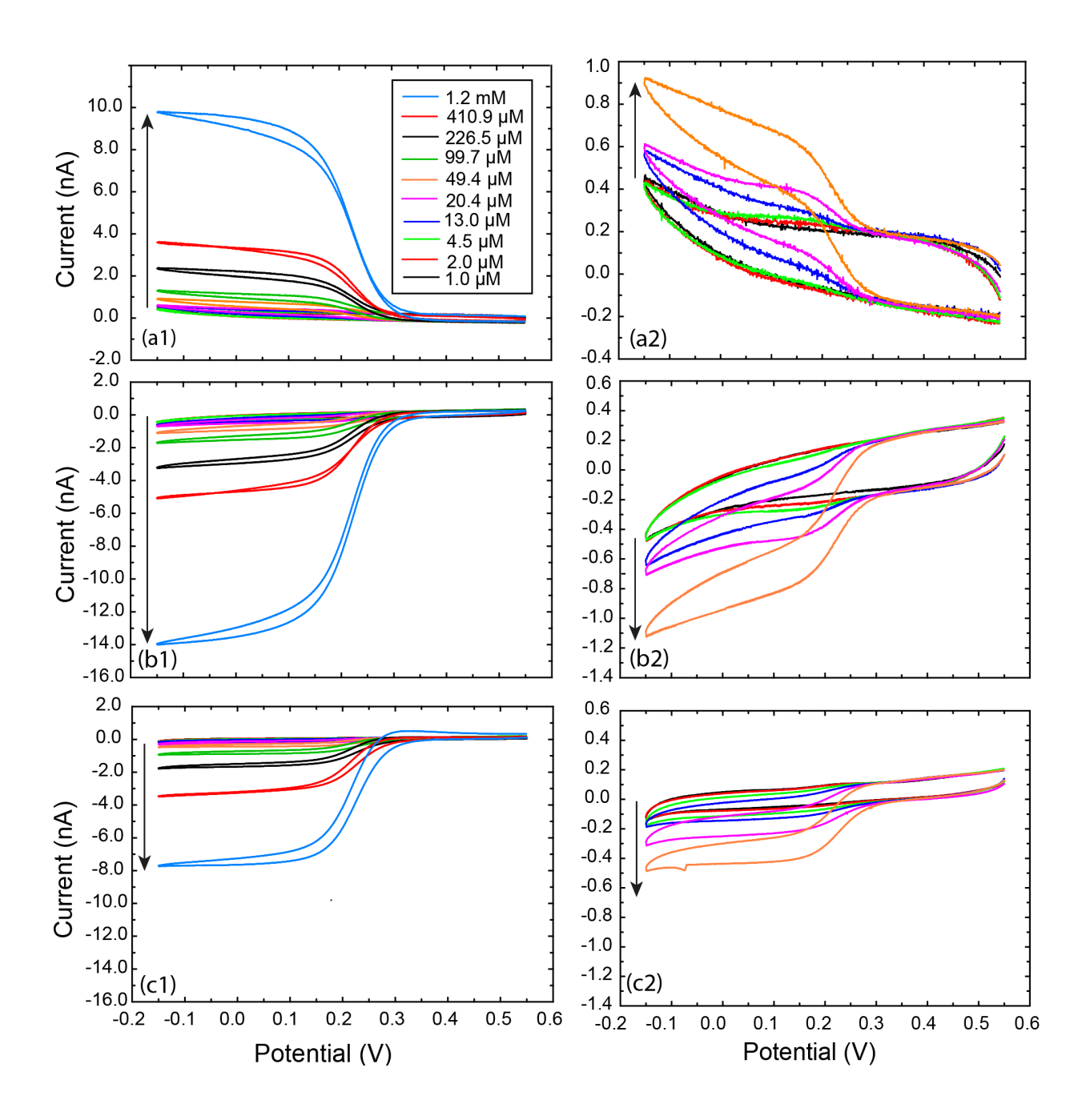


Figure 5

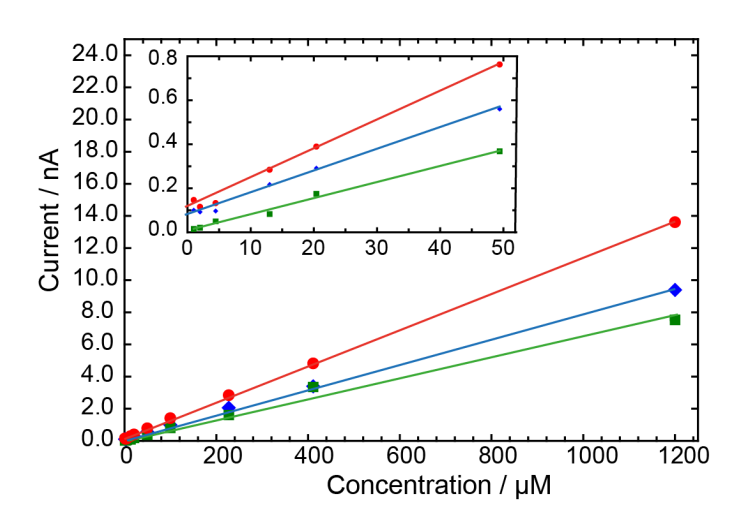


Figure 6

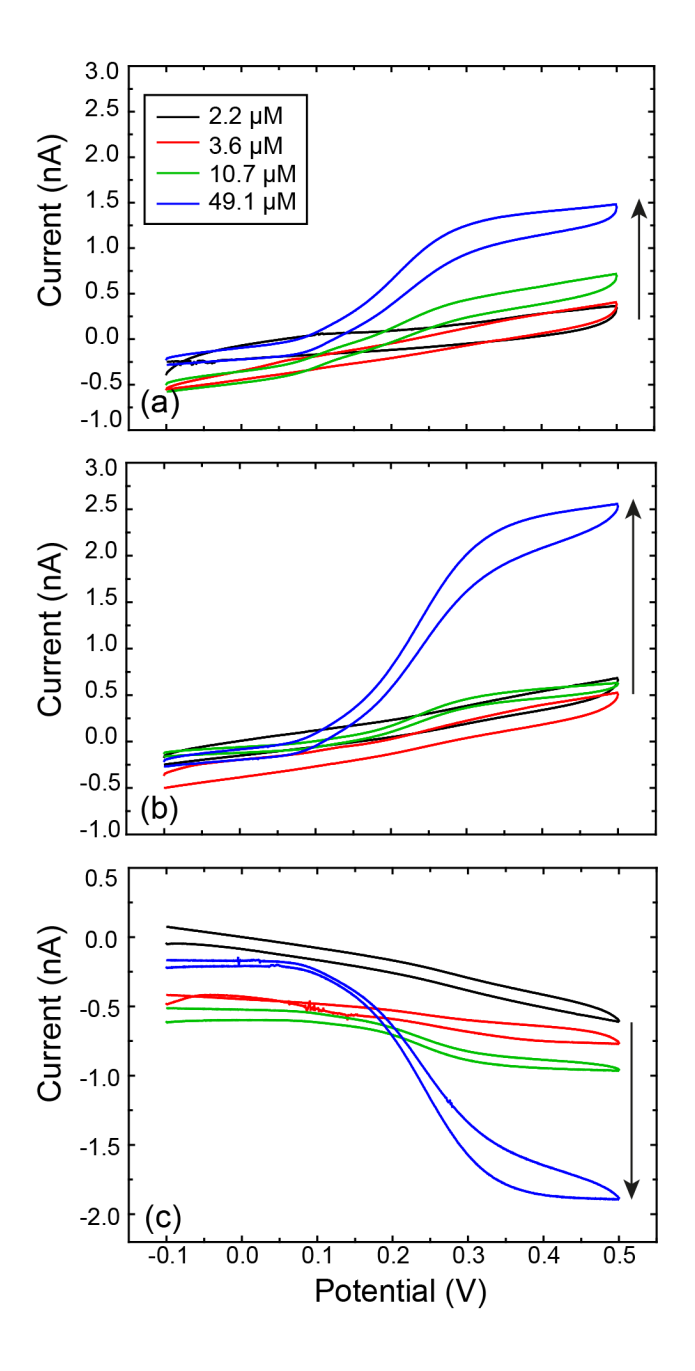


Figure 7

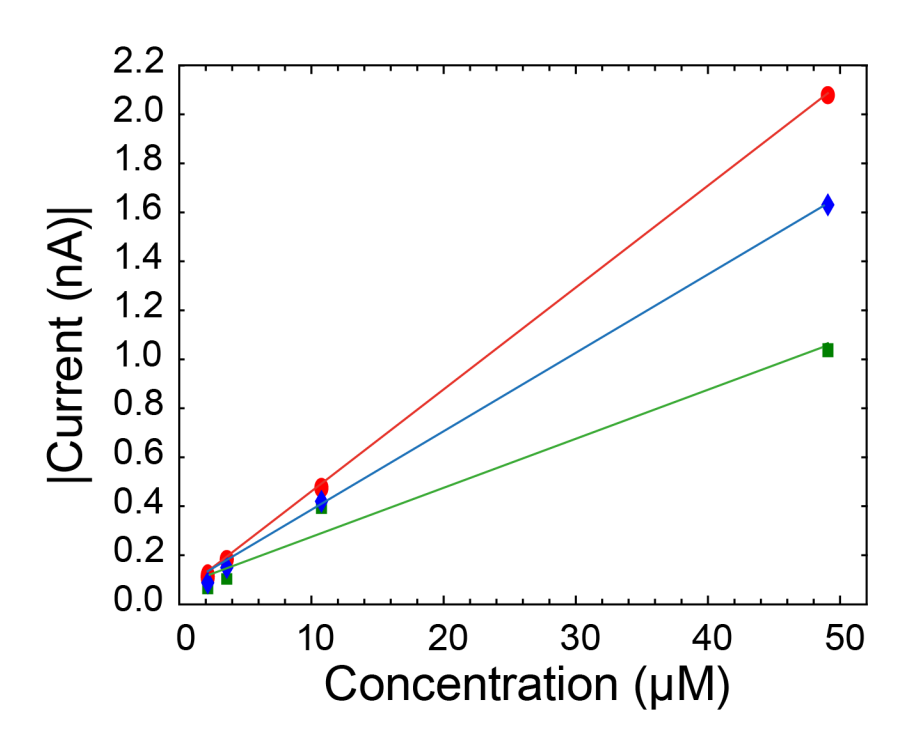


Figure 8

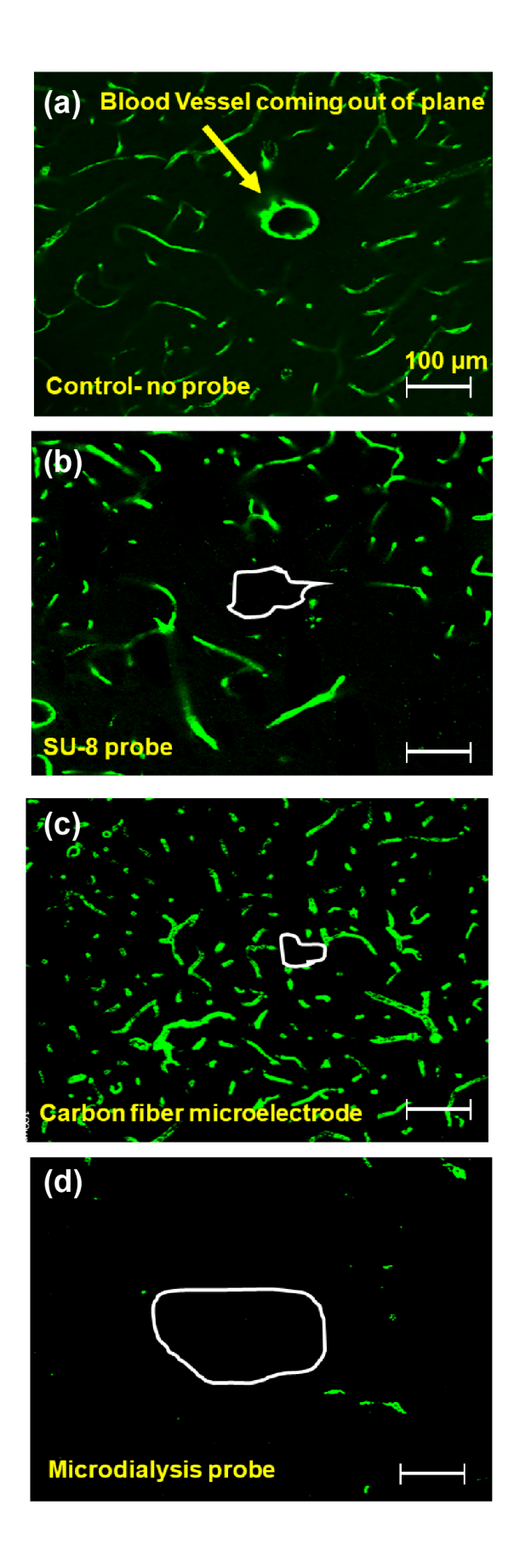


Figure 9

Supplementary Information

Miniaturized Probe on Polymer SU-8 with Array of Individually Addressable Microelectrodes

for Electrochemical Analysis in Neural and other Biological Tissues

Mahsa Lotfi Marchoubeh, a Samuel J. Cobb, Miguel Abrego Tello, Mengjia Hu, Andrea Jaquins

Gerstl, ^c Elaine M. Robbins, ^c Julie V. Macpherson, ^d Adrian C. Michael ^c and Ingrid Fritsch^a*

Department of Chemistry and Biochemistry, University of Arkansas, Fayetteville, 72701, USA, e)

f) Department of Chemistry, University of Cambridge, CB2 1EW, UK.

Department of Chemistry, University of Pittsburgh, Pittsburgh, PA, 15260, USA g)

Department of Chemistry and Centre for Doctoral Training in Diamond Science and Technology, h)

and Department of Physics, University of Warwick, Coventry, U.K.

*. To whom correspondence should be addressed

Tel: (479) 575-6499

Email: ifritsch@uark.edu

45

Supplementary Information

Supplementary information includes CV responses for individual electrodes in the ferricyanide solution.

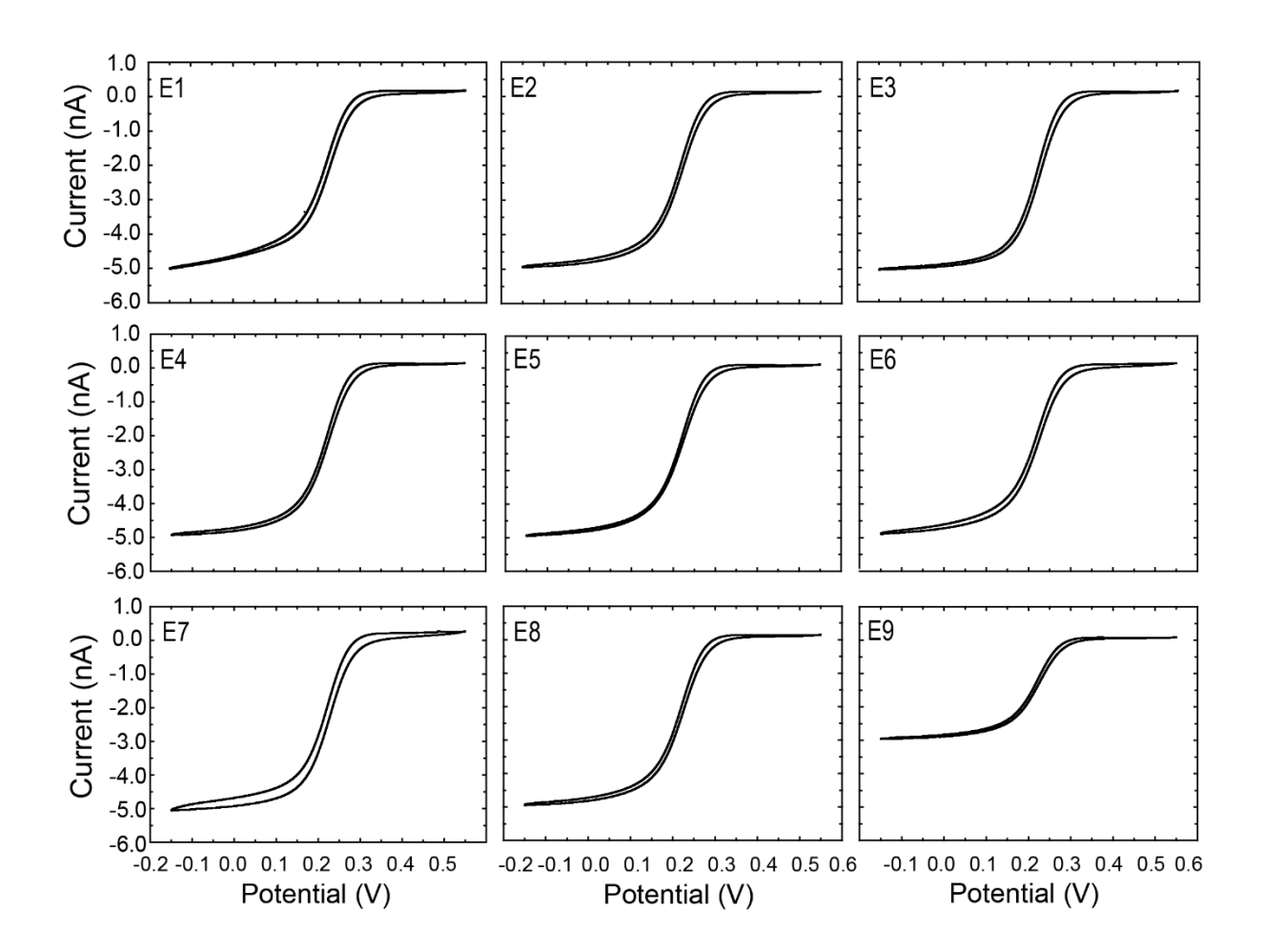


Fig. S1 CV responses at 0.020 V/s of individual electrodes on a probe in a solution of 1.02 mM $K_3Fe(CN)_6$ and 0.10 M KCl